LLNL-JRNL-403005

LAWRENCE
LIVERMORE
NATIONAL
LABORATORY

Hot electron energy coupling in ultra-intense laser matter interaction

A. J. Kemp, Y. Sentoku, M. Tabak

April 16, 2008

Physical Review Letters

Disclaimer

This document was prepared as an account of work sponsored by an agency of the United States government. Neither the United States government nor Lawrence Livermore National Security, LLC, nor any of their employees makes any warranty, expressed or implied, or assumes any legal liability or responsibility for the accuracy, completeness, or usefulness of any information, apparatus, product, or process disclosed, or represents that its use would not infringe privately owned rights. Reference herein to any specific commercial product, process, or service by trade name, trademark, manufacturer, or otherwise does not necessarily constitute or imply its endorsement, recommendation, or favoring by the United States government or Lawrence Livermore National Security, LLC. The views and opinions of authors expressed herein do not necessarily state or reflect those of the United States government or Lawrence Livermore National Security, LLC, and shall not be used for advertising or product endorsement purposes.

Hot electron energy coupling in ultra-intense laser matter interaction

A.J. Kemp[1], Y. Sentoku[2], and M. Tabak[1]
[1] *Lawrence Livermore National Laboratory, Livermore, CA*
[2] *University of Nevada, Reno, NV 89577*
(Dated: April 15, 2008)

We investigate the hydrodynamic response of plasma gradients during the interaction with ultra-intense energetic laser pulses, using one-dimensional kinetic particle simulations. As energetic laser pulses are capable of compressing the preformed plasma over short times, the coupling efficiency as well as the temperature of hot electrons drop, leading to localized heating near the point of absorption. We describe the cause of this drop, explain the electron spectra and identify the parametric region where strong compression occurs. Finally, we discuss implications for fast ignition and other applications.

While intense short laser pulses offer many interesting applications for high energy density physics [1], their interaction with dense plasma is poorly understood so that transport codes need to rely on simplified coupling models. In part, the complexity of the problem is caused by the several orders of magnitude between the dense-plasma response time and corresponding length and the scales of the laser spot size and pulse duration. In high-energy short pulse experiments, an additional problem is the large scale, low-density blow-off plasma in front of the actual solid target. It is created before the arrival of the main pulse by amplified spontaneous emission processes in the laser that cannot be easily suppressed, and is dense enough as to prevent light propagation several micrometers away from the target. As the formation of the preformed plasma occurs on a nanosecond time scale, it cannot be self-consistently included in the kinetic models that are currently used for short pulse interaction, because those are limited to picosecond time scales for technical reasons. Instead, the preformed plasma is usually modeled in separate hydrodynamic simulations. For a recent high energy short pulse experiment, scale lengths of about $0.5-1.0\,\mu$m between solid density and a fraction of the critical density $n_c = 1.1 \times 10^{21}\mathrm{cm}^{-3}$ were found, preceded by a longer scale length plasma [2]. For fast-ignition experiments, one expects scale lengths of up to $10\,\mu$m, depending on the energy in the pre-pulse.

This paper addresses the short-pulse laser driven dynamics of preformed plasma in the limit of intense, energetic pulses over a picosecond. At the onset of relativistic intensities $I_0 = 1.37 \times 10^{18}\mathrm{W/cm}^2$ the vacuum energy density of light corresponds to $\geq 300\,$Mbar at $1\,\mu$m wavelength light. Such a pressure can cause ions to move over several microns in less than 1 ps. Early works on absorption consider idealized step function density profiles, relatively short density gradients, or large volumes of [3, 4], effectively neglecting the large-scale ion motion. We characterize the response of plasma gradients to high intensity laser pulses $I_L \gg I_0$ in the limit of normal incidence with one spatial degree of freedom in a fully relativistic kinetic description. Our approach allows us to isolate 1D 'hydrodynamic'- from purely multi-dimensional effects, like beam filamentation [5], hole boring [6], and deformations of the plasma surface through Rayleigh-Taylor like instabilities [7]. While important for high intensity LPI, these effects naturally interplay with hydrodynamic aspects, making the full interaction not only complex and expensive to model because of its multi-scale nature. We ignore re-fluxing of hot electrons, which can occur due to electrostatic confinement in thin foils, or possibly in extremely resistive materials. We note that re-fluxing will likely cause higher coupling efficiencies and hot electron temperatures.

In the first part of this Letter, we consider two specific cases of plasma density gradients with different scale lenghts. Both cases show how the laser-generated pressure near the relativistic critical density causes a strong compression of the pre-plasma towards higher densities and acceleration of the plasma at lower densities into vacuum, followed by a drop in absorption and hot elec-

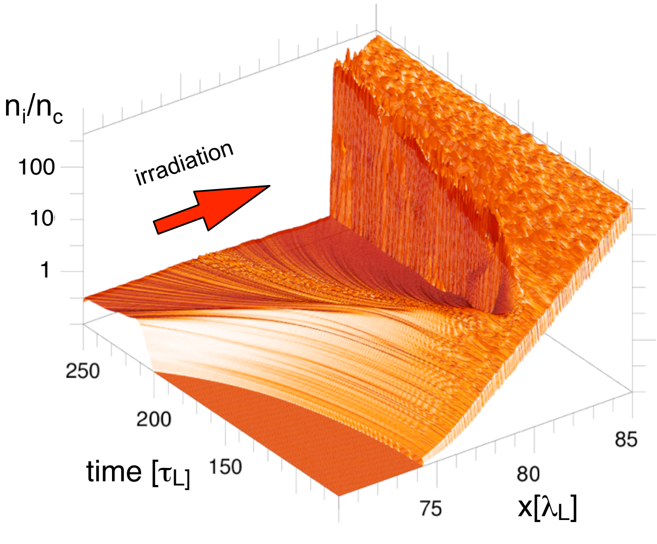

FIG. 1: Deformation of an exponential density gradient with scale length $l_s = 0.85\,\mu$m and peak density $n_{i,\max} = 400\,n_c$, irradiated by an ultra-intense laser pulse with $I_L = 10^{20}$ W/cm^2 and wavelength $\lambda_L = 1\,\mu$m.

tron temperature. To understand this, we study simple step function density profiles where the ion motion is suppressed. Here we find key properties of the laser-generated electron distribution at ultra-relativistic intensities; analytic expressions for cut-off energies and temperatures are given. Combined with an analytical description of the compression, which depends on plasma scale length, ion charge-to-mass ratio and laser intensity, wavelength and pulse duration, this is useful for defining plasma parameters at which absorption remains high over the laser pulse duration, and electron temperature is within the parameter band for fast ignition or other applications [1].

Our numerical tool is a one-dimensional particle-in-cell code [8]. We use a resolution of 500 cells per laser wavelength and about 300 particles per species and cell, and verified our results with 6× higher resolution, resolving the Debye length in the plasma at the highest density and initial temperature. Figure 1 describes the response of an exponential plasma profile during the interaction with an ultra-intense laser pulse. Shown is a contour plot of the ion density versus space and time for a gradient scale length of 0.85 μm, beginning at time $70\,\tau_L$, where $\tau_L \equiv \lambda/c \approx 3.3\,$fs is the laser period and $n_c = \pi\, m_e c^2/e^2\, \lambda^{-2}$ is the critical density. Between $90 - 100\,\mu$m the density profile is uniform, ending at the box boundary. Plasma ions have a mass $M_i = 8\, m_p$ where m_p is the proton mass and charge state $Z = 1$. A laser pulse enters the box at $x = 0$ with an intensity of 10^{20}W/cm^2 at $\lambda_L = 1\,\mu$m, and a semi-infinite pulse envelope. The vacuum region between the left box boundary and the plasma gradient allows for a free expansion over the simulation time of $350\,\tau_L$.

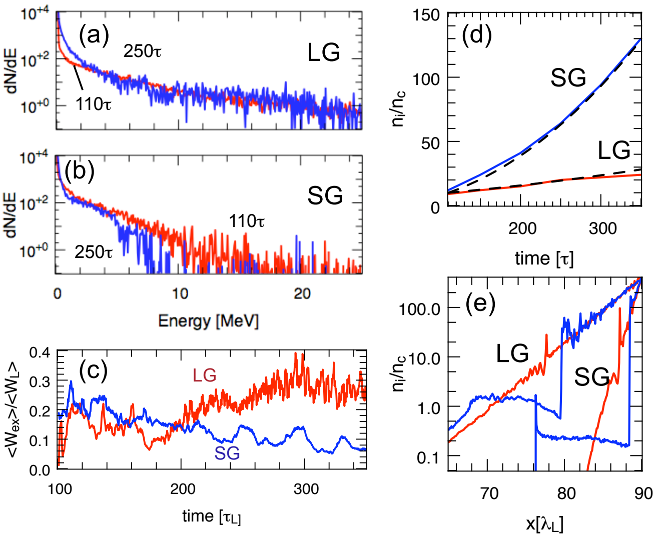

FIG. 2: Absorption and electron transport in exponential density gradients at $I_L = 10^{20}$W/cm^2. (a) Electron spectra at two times for a 'long gradient' (LG) case with $l_s = 3.25\,\mu$m; (b) for a 'short gradient' (SG) with $l_s = 0.85\,\mu$m; (c) electron energy flux density $< W_{ex} >_\tau$, normalized to the laser intensity W_L for SG and LG, recorded behind the density gradient at $x_0 = 95\,\mu$m; (d) density at the front, compared to the analytical result; (e) snapshots of ion density at $t = 110,\ 250\,\tau$.

Figure 2 gives details of the 'short gradient' (SG) case of Fig.1 and a 'large gradient' (LG) case with a scale length of 3.25 μm. Shown are snapshots of ion density, as well as corresponding electron spectra and fast electron energy flux density at $x = 95\,\mu$m

$$W_{e,x} = \sum_{x=x_d} n_e\,(\gamma - 1) v_x\ , \tag{1}$$

averaged over a laser cycle and normalized to the average laser energy flux $W_L = I_L/2$. We have checked that energy flux and spectra are independent of where exactly in the solid target region they are recorded. Additionally, spectra of all particles passing through a single cell over a $10\,\tau$ time interval give nearly identical results. In all simulations, energy is conserved up to xx% so that reflected flux is consistent with absorption. Figures 2(a,b) show electron spectra for the LG and SG cases at $I_L = 10^{20}$ W/cm^2 at two times, illustrating how they evolve from initially similar characteristics in temperature and number to quite different regimes at a later time, when hydrodynamics has changed the shape of the gradient. Fig.2(c) gives the time-dependence of the electron energy flux W_{ex}/W_L in both cases. Fig.2(e) shows corresponding ion density profiles at two times. In both cases, coupling of the intense laser pulse drives an electro-static shock wave towards the solid at a speed of $\approx 0.01c$ [9, 10], while it accelerates plasma towards vacuum. Two remarkable differences between these two cases are (a) an $\approx 5\times$ higher density of the 'lower shelf' plasma at $250\,\tau$ in the LG case and (b) its $\approx 5\times$ lower density of the 'upper shelf' plasma. These lead to significant differences in absorption, discussed below. Additional simulations at a hundred times reduced laser intensity show a much lesser impact on the plasma profile, leading to a nearly constant absorption of $\approx 30\%$.

The compression of the plasma gradient in Fig.2(e) can be described using momentum conservation near the front, i.e. where light is reflected [6, 7]

$$(1 + R) I_L/c = 2\, M_i\, u_f^2\, n_i \tag{2}$$

in a frame moving at velocity u_f with the front. Here $R \approx 1$ is the plasma reflectivity, I_L is the time-averaged laser intensity, and n_i is the ion density, neglecting the electron momentum. At relativistic intensities, reflection occurs at density $\gamma_{\rm os}\, n_c$ with $\gamma_{\rm os} = \sqrt{1 + (1 + R)\, a_0^2/2}$ [4, 6]. Below this density electrons are accelerated to energies $m_e\, c^2(\gamma_{\rm os} - 1)$ [7], consistent with the slopes observed in Fig.2(a,b). The time-dependent compression of a profile $n_i(x) = \gamma_{\rm os} n_c\, \exp[(x - x_c)/l_s]$ with a scale length l_s is obtained by solving Eq.(2) for u_f and integrating

$$x_f(t) = x_c + 2\,l_s\,\ln\left[1 + t\,\frac{c}{2l_s}\left(\frac{m_e}{2M_i}\,\frac{\gamma^2-1}{\gamma}\right)^{1/2}\right] \qquad (3)$$

to find the location of the front. Equation (3) is written in terms of $\gamma_{\rm os}$ using $I_L/c = m_e c^2 n_c\, a_0^2/2 = I_0\, a_0^2$ for $\lambda = 1\,\mu$m. Figure 2(e) plots the corresponding interface density at the front vs. time and simulation results. Expansion of the plasma towards vacuum is characterized by that fact that the outward accelerated mass is nearly constant, and by $v_i \propto (x - x_c) \times (t - t_0)$. The ion bump at the front of the expansion has been discussed earlier [11].

In order to understand the evolution of absorption and electron flux in the density gradients above, we turn to a 'quasi-static' scenario in which the ion motion is suppressed. Instead of an exponential ramp, we use a $3\,\mu$m layer of plasma at uniform ion density n_s in front of a $10\,\mu$m layer of plasma at 'solid' density $200\,n_c$. Figure 3(a,b) shows electron spectra, cycle-averaged electron energy flux W_{ex}/W_L, as well as the electrostatic field near the boundary for several 'lower shelf' densities n_s/n_c.

The location of the lower shelf is indicated by a shadow in Fig.3(b). Charge density can be inferred from $\partial E_x/\partial x = 4\pi\rho$. For $n_s \geq 1$, hot electrons in the lower shelf cause an ambipolar field E_x and a tail in the distribution function [7] that is absent for smaller n_s. This limiting value $n_s^{\rm max}$ can be determined by an energy balance between the laser field and the electrostatic field in the shelf

$$2\,I_L/c = e\,n_s\,\phi_s\ , \qquad (4)$$

with $\phi_s = 2\pi\,e\,n_s\,l_s^2$. Normalization yields $a_L^2 = 2\pi^2\,(n_s/n_c)^2\,(l_s/\lambda)^2$. For $a_L = 10$ and $l_s = 3\mu$m, we find $n_{s,0} = 0.75\,n_c$. On the other hand, by fixing $n_s = n_c$ we get a maximum shelf length of $2.25\,\mu$m, consistent with Fig.3(b). Here E is scaled with $E_0 = m_e\omega\,c/e$. The maximum electric field at the interface $E_{x,{\rm i}}^{\rm max} = a_0/\sqrt{2}$ is reached when the shelf arial density $n_s\,l_s$ of Eq.(4) is 'critical', which also agrees with Fig.3(b), after accounting for some absorption; see Fig.3(c).

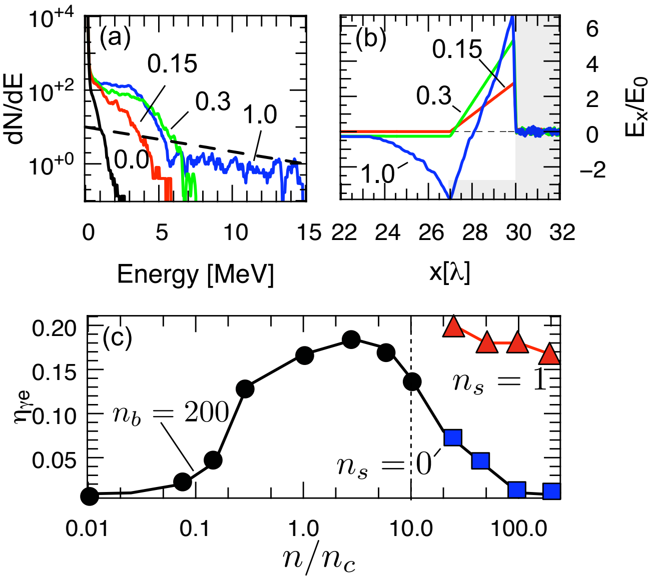

FIG. 3: Absorption and electron transport in static step-function density profiles at $I_L = 10^{20}$W/cm^2. (a) Electron spectra for various values of the 'shelf density' parameter n_s as indicated. Dashed line gives a 6.5 MeV slope consistent with [7]; (b) corresponding snapshots of E_x; location of shelf and bulk target are indicated by shadow; (c) laser-to-electron coupling efficiency vs. plasma density. For $n_s \leq 10$, targets consist of a $3\,\mu$m long 'lower' shelf at density n_s followed by $10\,\mu$m of plasma at $200\,n_c$; for $n_s \geq 10$ the plasma is uniform.

Electron spectra in the quasi-static scenario depend mostly on the pre-plasma, or in other words, on the electrostatic field $E_{x,i}$ at the interface with the bulk target. Key features are reproduced by a simple model of electron acceleration near the interface under the condition that the lower shelf is just critical. Laser electric and magnetic field in vacuum near an almost perfectly reflective boundary at density n_p are given by [12]

$$\begin{aligned} E_y &= 2\,a_0 \sin(kx + \phi)\,\cos(\omega\,t)\ , && (5)\\ B_z &= 2\,a_0 \cos(kx + \phi)\,\sin(\omega\,t)\ , && (6) \end{aligned}$$

where $\tan(\phi) = -\sqrt{n_c/n_p}$. An electron at $(x, t) = (0, 0)$ is extracted by the longitudinal electric field and gains negative (mostly) transverse momentum until the longitudinal component of the Lorentz force exceeds E_x. The time t' at which the particle turns around can be found by integrating the equation of motion $\partial u_x/\partial t = -2\pi E_x + 4\pi\, a_0\, \sin(\omega t)$, assuming that $v_y \approx c$. Solving for $u_x(t') = 0$, we find $t' \approx 0.12$. After this time no further particles can be extracted. Electrons at $x' = -t'$ are now accelerated by the Lorentz force towards the boundary over the same time interval, so that they gain a longitudinal momentum not larger than

$$u_x^{\rm max} = 4\pi\, a_0\, t' \approx 1.45\, a_0\ . \qquad (7)$$

For $a_0 = 10$ this expression predicts a cutoff energy $E_{\rm max} \approx 7\,$MeV, in agreement with Fig.3(a). The shoulder-like feature of the spectrum stems from (i) electrostatic shielding of electrons extracted during the time interval $[0, t']$ by the charges of other electrons and (ii) their relative phase w.r.t. the EM field pattern. For large amounts of 'lower shelf' plasma, the shoulder of the spectrum is independent of the amount of plasma, while the maximum electron energy in the shoulder scales linear with laser amplitude. For an under-critical lower-shelf, where E_x is determined by the arial charge $n_s\,l_s$, the spectrum is independent of intensity. This has been verified by a simulation similar to the one labeled '0.1' in Fig.3(a) but with a laser amplitude $a_0 = 20$, giving an almost identical electron spectrum. The extraction/acceleration process repeats itself at time $\tau/2$ with $u_y > 0$, leading to the well-known $2\omega_0$ electron jets [3]. Without the lower shelf there is no positive electrostatic field, i.e. no extraction, so that transverse acceleration occurs in the evanescent mode of E_y, leading to much smaller absorption.

Figure 3(c) plots time-averaged electron flux (absorption) vs. plasma density in a combination of two separate scenarios: at low density $n/n_c < 10$, density refers to a $3\,\mu$m thick 'lower shelf' preceding $10\,\mu$m of bulk plasma at a constant density of $200\,n_c$, compare Fig.3(a). The intense laser pulse propagates through the lower shelf plasma because it is relativistically under-critical [4]. For higher densities $n/n_c \geq 10$, the plasma becomes opaque for the intense laser. Here, density refers to a $10\,\mu$m thick uniform plasma layer; both scenarios give the same result for $10\,n_c$. The effect of changing the bulk plasma density at a fixed value of $n_s = 0.1\,n_c$ is small, as shown in a separate curve. This demonstrates that absorption depends mostly on the lower shelf density where one is present, and drops with bulk density with small amounts of preplasma. Figure 3(c) is representative of the decreasing absorption seen in Fig.2, where the 'lower shelf' density drops due to the hot electron pressure, while the interface is compressed over time. In one spatial dimension, this effect can only be slowed down by choosing larger gradient lengths for the preformed plasma, i.e. more energy in the prepulse, or lower intensities.

A fiducial simulation of a step function density profile with mobile ions at a density $100\,n_c$ and an intensity $I_L = 10^{18}\mathrm{W/cm}^2$ yields an absorption fraction of 14 % for an initial electron temperature 10 keV, which agrees well with results published earlier [3]. This relatively high value is caused by thermal expansion of the bulk plasma and the subsequent formation of a density gradient similar to the ones discussed above. However, in runs with initially cold electrons, i.e. $T_{e,0} < 1\,\mathrm{keV}$, or at intensities around $10^{20}\,\mathrm{W/m}^2$ the expansion is suppressed by the ponderomotive pressure and absorption drops to $< 1\%$. We find that the initial electron temperature is much less relevant in our density gradient simulations.

While collisions play no direct role for absorption in plasma density gradients around $10-30\,n_c$ and keV temperatures, they could contribute indirectly by causing strong electrostatic fields in highly resistive material in dense plasma. This could cause the re-fluxing of hot electrons even in large FI-relevant targets, and enhance absorption and electron temperature. Results are scalable w.r.t. laser wavelength using the relation $I\,\lambda^2 \propto a_0^2$, i.e. for a given intensity a smaller wavelength leads to smaller a_0. While our study addresses normal incidence, absorption for finite angles of incidence tends to be much higher because of the longitudinal field component in the laser pulse [13, 14]. This will affect the momentum balance Eq.(2). For small angles, both the normal Poynting flux and and critical density are reduced by a factor $\cos\alpha$ so that we do not expect drastic changes. Two dimensional studies of angle dependence are in progress.

In conclusion, preformed plasma is beneficial for high absorption at MeV electron energies in ultra-high intensity short-pulse laser experiments. At intensities $I_L \gg 10^{18}\mathrm{W/cm}^2$ the ponderomotive pressure, exerted via an ambipolar electrostatic field around the point of absorption, compresses plasma at densities greater than the critical density leading to a steepening of the interface. At the same time, it accelerates low-density plasma away from the interaction region and thereby reduces absorption over a time scale determined by the plasma gradient length and laser parameters, typically sub-ps. Recent experiments at ultra-high intensities have demonstrated the positive effect of preformed plasma on achieving high absorption [15], and that the compression of preformed plasma by high-energy pulses can lead to dominant coupling into a cold electron population [16], as well as laser-driven shock waves [17].

A.K. acknowledges discussions with M.Key, W.Kruer, H.Ruhl, and S.Wilks.

Work was performed under the auspices of the U.S. Department of Energy by the Lawrence Livermore National Laboratory under Contract No. W-7405-ENG-48.

Prepared by LLNL under Contract DE-AC52-07NA27344

[1] M. Tabak, J. Hammer, M. Glinsky, W. Kruer, S. Wilks, J.Woodworth, E. Campbell, M. Perry, and R. Mason, Phys. Plasmas **1**, 1626 (1994).
[2] W. Theobald and K. Akli, Phys Plasmas (2006).
[3] W. Kruer and K. Estabrook, Phys. Fluids **28**, 431 (1985).
[4] E. Lefebvre and G. Bonnaud, Phys. Rev. Lett. (1995).
[5] A. Pukhov and J. Meyer-ter-Vehn, Phys. Rev. Lett. **76**, 3975 (1996).
[6] Y. Sentoku, W. Kruer, M. Matsuoka, and A. Pukhov, Fusion Science and Technology **49**, 278 (2006).
[7] S. Wilks, W. Kruer, M. Tabak, and A. Langdon, Phys. Rev. Lett. **69**, 1383 (1992).
[8] R. Pfund, R. Lichters, and J. Meyer-ter-Vehn, in *Superstrong Fields in Plasmas*, edited by M. Lontano et al. (American Institute of Physics, New York, 1998), vol. 426 of *AIP Conf. Proc.*, p. 141.
[9] L. Silva, M. Marti, J. Davies, et al., Phys. Rev. Lett. **92**, 015002 (2004).
[10] J. Denavit, Phys. Rev. Lett. **69**, 3052 (1992).
[11] A. Gurevich and A. Meshcherkin, Sov. Phys. JETP **53**, 937 (1981).
[12] M. Born and E. Wolf, *Principles of Optics* (Pergamon, New York, 1975).
[13] F. Brunel, Phys. Rev. Lett. **59**, 52 (1987).
[14] P. Gibbon and A. Bell, Phys. Rev. Lett. **68**, 1535 (1992).
[15] Y. Ping, R. Shepherd, et al., Phys. Rev. Lett. **100** (2008).
[16] B. Chrisman, Y. Sentoku, A. Kemp, et al., Phys. Plasmas **x**, xxx (2008).
[17] K. Akli et al., Phys. Rev. Lett. **x**, xxx (2008).